Chemical Engineering Journal 508 (2025) 160990

Contents lists available at ScienceDirect

Chemical Engineering Journal

journal homepage: www.elsevier.com/locate/cej

A study on iron-composite polymer propellants for improved plasma generation in electric propulsion systems

Chao-Wei Huang [a], Ping-Han Huang [b], Zong-Ying Yang [c], Yueh-Heng Li [b,c,d,*]

[a] Department of Engineering Science, National Cheng Kung University, Tainan 70101, Taiwan
[b] Department of Aeronautics and Astronautics, National Cheng Kung University, Tainan 70101, Taiwan
[c] International Master Degree Program on Energy Engineering, National Cheng Kung University, Tainan 70101, Taiwan
[d] Institute of Space Systems Engineering, National Cheng Kung University, Tainan 70101, Taiwan

ARTICLE INFO

Keywords:
Electric propulsion
Pulsed plasma thruster
Metal-composite polymer
PMMA
Iron powder
Thrust-to-power ratio

ABSTRACT

Pulsed plasma thrusters (PPTs) are widely employed in CubeSats due to their compact size, simplicity, and ability to generate small and precise thrust. However, their low efficiency and thrust-to-power ratio limit broader adoption. This study introduces a novel PMMA-based metal-composite polymer propellant (PMMA@Fe) doped with iron powder to replace the conventional PTFE propellant. PMMA@Fe samples with iron powder concentrations ranging from 5 wt% to 20 wt% were synthesized and evaluated. The addition of iron powder reduced plasma impedance and increased discharge currents, resulting in a 62.5% improvement in impulse bit (from 80.3 μNs to 131.9 μNs) and a 63.5% enhancement in the thrust-to-power ratio (from 17.8 μN/J to 29.3 μN/J) when compared to pure PMMA.

Material characterization revealed that the ablation rate of PMMA@Fe increased from 4.6 μg/shot (pure PMMA) to 8.2 μg/shot (5 wt% Fe) and plateaued at higher concentrations. Plasma plume analysis confirmed a 50 % increase in plasma generation as the iron content rose to 20 wt%, supported by a 40 % increase in optical emission intensity of PMMA decomposition species. Despite the enhanced performance, high iron content (≥15 wt%) led to irregular discharges and carbon–metal deposition, limiting the thruster's operational lifespan to 6,000 discharges.

The study concludes that the PMMA@Fe propellant with 15 wt% iron offers an optimal balance, achieving 18.7 % thrust efficiency and a specific impulse of 1,324 s, while maintaining structural integrity. These findings demonstrate the potential of PMMA@Fe to enhance PPT performance for CubeSat applications.

1. Introduction

With the rapid development of the space industry, propulsion technology has become a critical component of the space sector, playing an indispensable role in diverse missions. For example, Taiwan's Formosat-7 program employs satellite propulsion systems for orbit maintenance and fine-tuning, ensuring continuous and precise data collection by scientific instruments [1]. Similarly, NASA's DART (Double Asteroid Redirection Test) mission demonstrated the use of propulsion systems to alter a spacecraft's trajectory, providing technical validation for asteroid deflection and planetary defense [2].

Propulsion systems can be broadly categorized into chemical and electric propulsion, differentiated by their trade-off between thrust and efficiency. Chemical propulsion, relying on chemical fuels, delivers high thrust suitable for rapid acceleration or heavy payload launches, with specific impulses typically ranging from 200 to 500 s [3]. Conversely, electric propulsion systems achieve high efficiency and specific impulses of 1,500 to 3,000 s by ionizing fuel to generate plasma and accelerating ions through electric and magnetic fields. This process efficiently converts external energy sources, such as solar or electrical power, into the propellant's kinetic energy, significantly enhancing exhaust velocity and specific impulse (Isp) [4,5].

Currently, electric propulsion systems for small satellites include ion thrusters, Hall effect thrusters, magnetoplasmadynamic (MPD) thrusters, and pulsed plasma thrusters (PPTs), each suited for different performance requirements. Ion thrusters operate with thrust ranges of 10–100 mN, specific impulses of 1,500–3,000 s, and power requirements of 10–50 W, ideal for high-efficiency, low-thrust missions [6–8]. Hall

* Corresponding author at: Department of Aeronautics and Astronautics, National Cheng Kung Univ., Tainan 701, Taiwan.
E-mail address: yueheng@mail.ncku.edu.tw (Y.-H. Li).

https://doi.org/10.1016/j.cej.2025.160990
Received 23 December 2024; Received in revised form 9 February 2025; Accepted 24 February 2025
Available online 24 February 2025

Table 1
Summary of pulsed plasma thruster.

Literature	Propellant	I_{sp} (s)	I_{bit} (μNs)	η (%)	Thrust-to-power ratio (μN/W)
PPTCUP [22]	PTFE	655	40	5.7	20
BMP-220 [23]	PTFE	—	20	—	—
Tokyo Metropolitan Univ. [24]	PTFE	300–320	140–1460	4.3–11.1	15–70
Osaka Univ. [25]	PTFE	460–500	190–670	10.0–14.0	40–45
UIUC PPT-7 [26]	PTFE	330–570	250–2590	—	25–45
Princeton Univ. [27]	PTFE	300–3200	300–3200	2–9	12–45

effect thrusters provide thrust from a few mN to 1 N and specific impulses of 1,000–3,000 s, with power requirements of 100 W–20 kW, often used for geostationary orbit transfers [9–13,47]. MPD thrusters, offering thrust of 1–10 N and specific impulses of 1,000–2,000 s, require hundreds of kilowatts, making them suitable for larger spacecraft but unsuitable for small satellites [14].

In contrast, PPTs are electromagnetic propulsion systems distinguished by their simplicity, compactness, and low power requirements (1–10 W). With a thrust range of 10–100 μN and specific impulses of 600–1,200 s, PPTs are well-suited for small satellites, particularly CubeSats, which are standardized cubic satellites widely used for academic research and technology demonstrations [15,16]. CubeSats benefit from propulsion systems for expanded functionalities such as orbit maintenance, attitude control, formation flying, and end-of-life deorbiting [6,17,18].

The PPT's reliance on solid propellants provides additional safety and design advantages, including longer storage life and operation across a wide temperature range, while eliminating the need for bulky gas storage containers. These characteristics make PPTs a compelling choice for CubeSat applications, particularly in power-constrained scenarios, outperforming ion and Hall effect thrusters in terms of lightweight design and operational simplicity [19].

Despite these advantages, PPTs face criticism for their low efficiency and thrust-to-power ratio, with an average efficiency of approximately 10 % [20,21]. Table 1 summarizes various PPTs developed for CubeSats, highlighting their efficiency, thrust-to-power ratios, and propellants used, emphasizing ongoing efforts to improve their performance and address these limitations.

The efficiency and performance of a PPT are influenced not only by its structural geometry and electrode configuration [28,29] but also significantly by the propellant system. The material, geometry, and feed mechanism of the propellant [30–33] can greatly affect its ablation behavior, which in turn impacts thrust, efficiency, and the thrust-to-power ratio.

For instance, Tahara *et al.* (2007) replaced the conventional polytetrafluoroethylene (PTFE) with ethylene-tetrafluoroethylene (ETFE) as the propellant and observed a marked improvement. ETFE demonstrated a higher specific impulse (570 s vs. 320 s for PTFE) and greater thrust efficiency (17.2 % vs. 12.6 %), although its thrust-to-power ratio was only 75 % of that of PTFE [34].

Similarly, Glascock *et al.* (2020) investigated the use of HIPEP, a propellant synthesized by crosslinking hydroxylammonium nitrate (HAN) and polyvinyl alcohol (PVA). HIPEP exhibited an ablation rate twice that of PTFE when subjected to DC discharges for gas generation. However, despite the enhanced ablation rate, the impulse bit did not show significant improvement, attributed to HIPEP's high hygroscopicity during manufacturing, which led to suboptimal results [35].

Hideto *et al.* (2006) explored a propellant based on hydroxyl-terminated polybutadiene ammonium perchlorate (HTPB-AP), finding that its thrust-to-power ratio exceeded that of PTFE. In a configuration of HTPB/AP/Al = 20/80/20, the specific impulse was 1.8 times greater than PTFE, and propulsion efficiency was twice as high. However, the potential production of harmful substances during manufacturing limited its practical application [36].

Given this context, the present study proposes a novel metal-composite polymer propellant, using polymethyl methacrylate (PMMA) mixed with iron powder (PMMA@Fe) as the propellant for PPTs. Both PMMA and PTFE possess excellent electrical properties, such as high dielectric strength and stable insulating characteristics. However, PMMA offers additional advantages, including resistance to environmental moisture, cost-effective manufacturing, and non-toxicity, ensuring environmentally safe PPT operation.

The study focuses on improving the propulsion performance of PMMA by doping it with iron powder. The high mass of iron atoms contributes directly to momentum generation, as momentum is proportional to mass. During acceleration, this characteristic is expected to enhance thrust. Moreover, the low ionization energy of iron (7.87 eV) facilitates ionization during arc discharges, increasing the density of high-energy plasma particles and improving plasma generation efficiency.

The addition of iron powder is anticipated to alter the plasma's overall properties, reducing plasma impedance in the PPT chamber. This change enhances the arc current and strengthens the Lorentz force, ultimately improving propulsion performance. These improvements are expected to position PMMA@Fe as a promising candidate for next-generation PPT propellants.

2. The thrust estimation for PPT

The thrust of PPT is defined as follows. F_{EM} is the electromagnetic force and F_{ET} is the thrust contributed by the gas dynamic expansion [37]

$$F = F_{EM} + F_{ET} \tag{1}$$

The impulse bit can also be defined as the following [28]

$$I_{EM} = \frac{u_0}{2}\frac{h}{w}\int_0^t i^2 dt \tag{2}$$

$$I_{ET} = \left[\frac{8(\gamma-1)}{\gamma^2(\gamma+1)}\cdot m\cdot E\right]^{\frac{1}{2}} \tag{3}$$

Here, u_0 is the permeability of the vacuum, and h and w represent the distance between the electrodes and the width of the electrodes, respectively. $\int_0^t i^2 dt$ is the integral of the square of the discharge current over time. Since γ is the ratio of specific heat for a material, it will be defined later based on the propellants used in this experiment with different iron powder doping ratios. m represents the mass of the propellant consumed, and E is the input energy.

Specific impulse (I_{sp}) and thrust efficiency (η_t) are crucial parameters for evaluating the performance of a thruster. These parameters can be estimated from the impulse bit (I_{bit}), mass shot (Δm), input energy (E), and gravitational acceleration (g) as follows [38];

$$I_{sp} = \frac{I_{bit}}{\Delta m g} \tag{4}$$

Thrust efficiency reflects how effectively the input energy (E) is converted into useful mechanical energy (thrust). It can be expressed as:

$$\eta_t = \frac{\frac{1}{2}\Delta m\left(gI_{sp}\right)^2}{E} \tag{5}$$

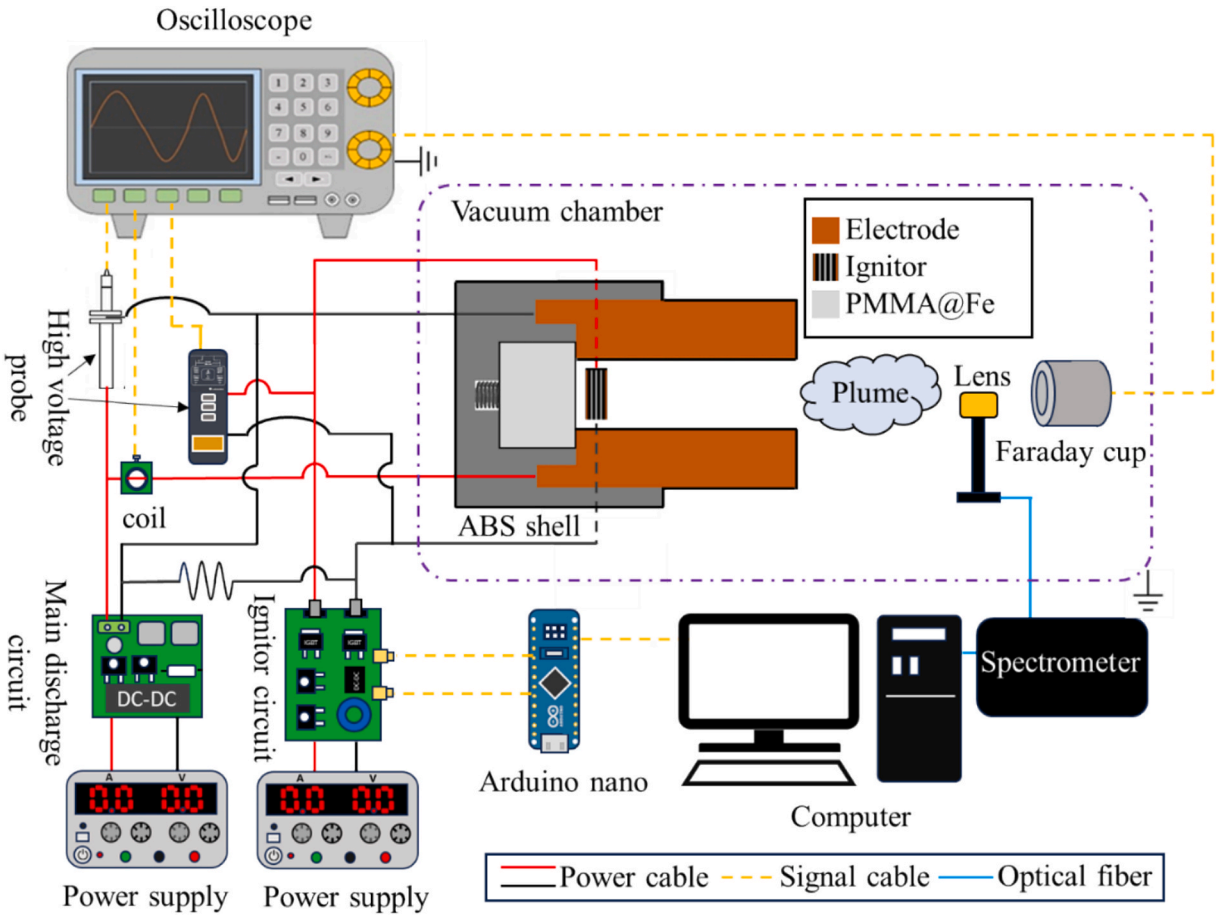

Fig. 1. Diagram of the experiment setup.

3. Experimental setup

Fig. 1 shows the experimental setup for the pulsed plasma thrusters (PPT), which consists of four main systems: the propulsion system, power system, measurement system, and vacuum system. The propulsion system includes a parallel PPT with copper (Cu) electrodes, each measuring 47 mm in length and 10 mm in thickness, with a 10 mm gap between the electrodes. The ignitor is positioned on the sidewall of the thruster to provide the initial plasma needed for discharge. The propellant used in the experiment is PMMA@Fe, containing varying weight percentages of iron powder (details are provided in Section 3-1), which serves as the variable to study its effect on thruster performance. The thruster structure and its physical images are shown in Fig. 2 and Fig. 3.

The power system consists of two key circuits: an inductive energy storage ignition circuit [39,40], which provides the initial energy for ignition, and a high-voltage discharge circuit, which supplies continuous energy during the discharge process. Both circuits are custom-developed in our laboratory. The power supply is sourced from a standard power supply to ensure stable energy delivery. The measurement system integrates several devices to precisely record system parameters. A high-voltage probe (DP-15 K, RIGO, Taiwan) and a Rogowski coil (CURRENT MONITOR 301X, Pearson Electronics, USA) are used to measure the voltage and current in the experiment, allowing for the estimation of propulsion performance. Additionally, a Faraday cup, developed in our laboratory [41], is used to collect and analyze the plasma plume. By measuring the voltage difference across the resistor in the circuit, the current of the plasma plume is calculated. To exclude electrons and only collect ions, a negative bias voltage of −70 V is applied to the Faraday cup to prevent potential shielding due to the current flowing through the resistor. The resistor used in this experiment is 680 Ω. The experiment was conducted at a pressure below 2×10^{-6} [torr] to simulate the space environment.

3.1. Preparation and characteristics of PMMA@Fe

The PMMA@Fe samples were prepared using a casting method. Initially, 20 g of polymethyl methacrylate (PMMA) pellets were dissolved in 60 mL of ethyl acetate under stirring at 500 rpm and 40 °C for 6 h until fully dissolved. Subsequently, 1.05, 2.2, 4.12, or 5.05 g of iron powder were added to achieve the desired Fe doping ratios (5, 10, 15, and 20 wt%). The mixture was stirred at 500 rpm for an additional 3 h to ensure uniform dispersion, forming the precursor solution. The solution was then cast into silicone molds and dried in an oven at 50 °C for 36 h until the solvent was completely removed. After drying, the samples were left to rest at room temperature for 24 h before being demolded. The synthetic procedure for PMMA@Fe is illustrated in Fig. 4, and a series of propellant samples with different iron doping ratios (5, 10, 15, and 20 wt%) are shown in Fig. 5, with their respective densities listed in Table 2. Detailed experimental conditions are listed in Table 3.

The ratio of specific heat (γ) mentioned in Equation (3) is defined as the ratio of the specific heat at constant pressure (C_p) to the specific heat at constant volume (C_v). Mathematically, it is expressed as

$$\gamma = \frac{c_p}{c_v} \tag{6}$$

For polymethyl methacrylate (PMMA), Choy, C.L. [42] finds the relation between C_p and C_v.

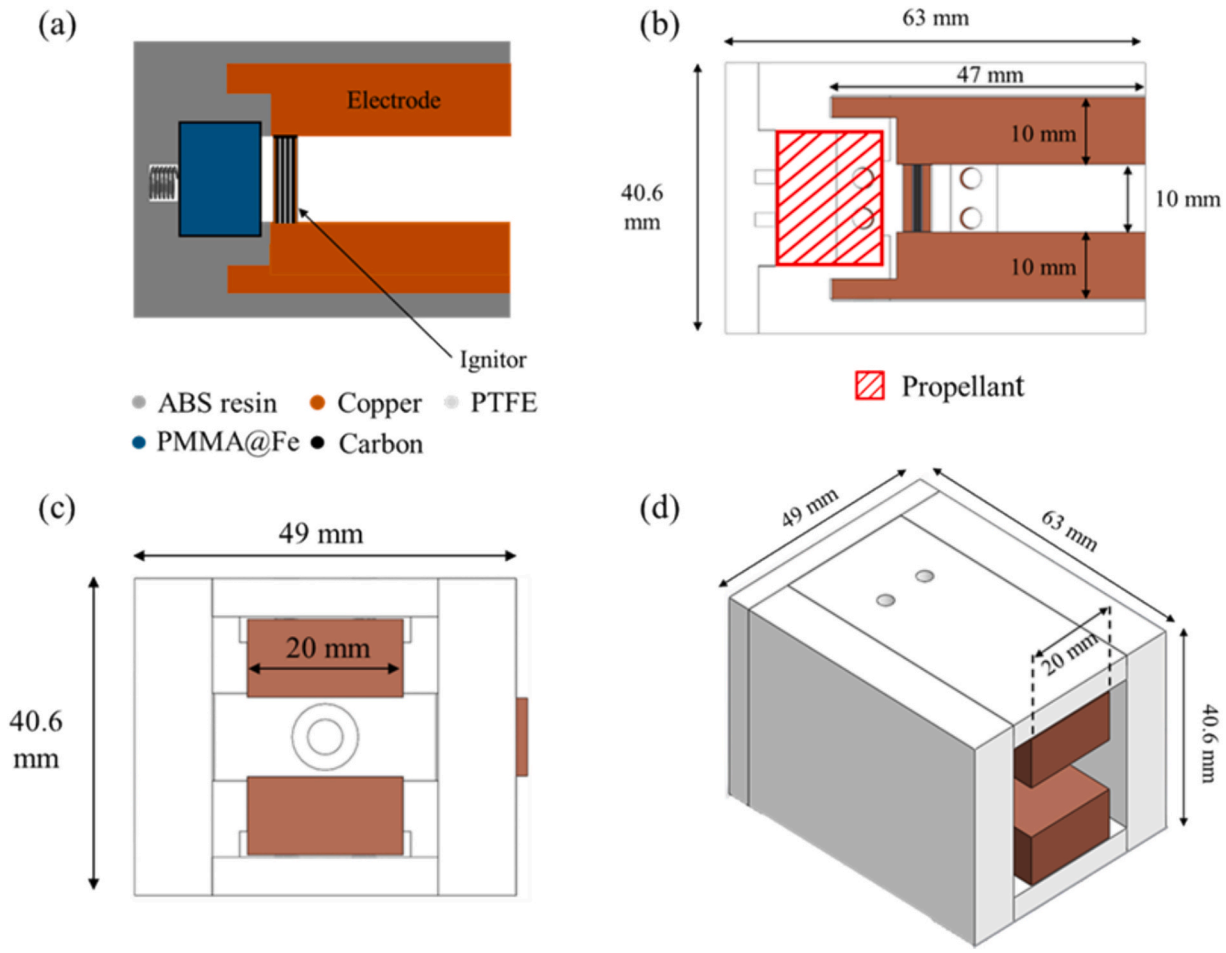

Fig. 2. Design of thruster (a) schematic diagram (b) sectional view (c) front view (d) isometric view.

Fig. 3. Diagram of the pulsed plasma thruster.

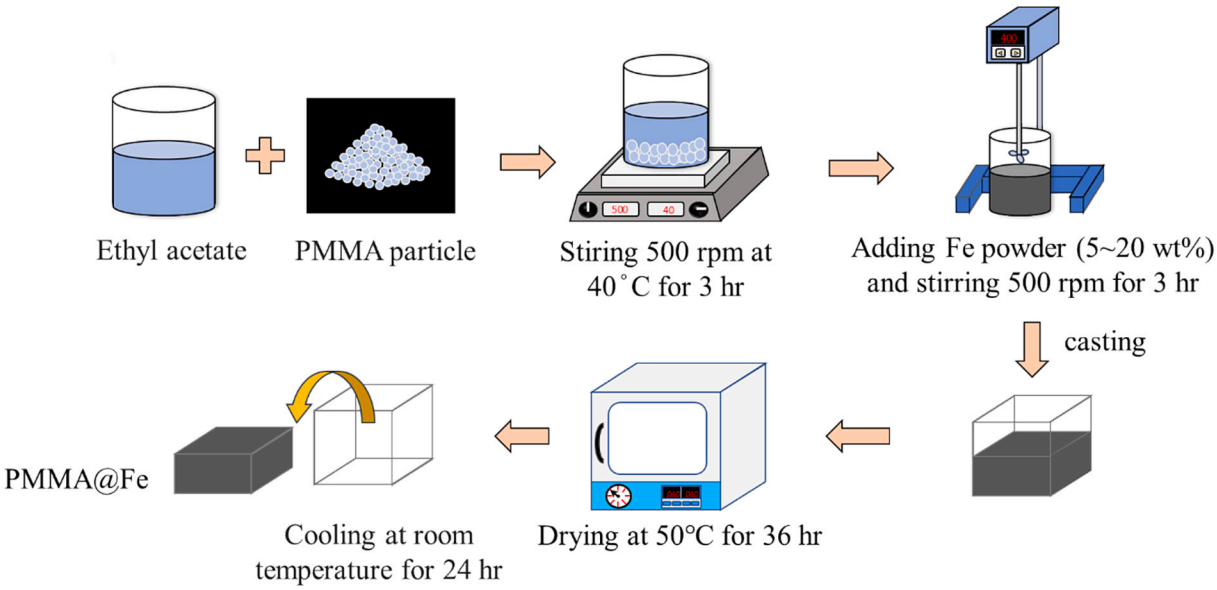

Fig. 4. The synthetic routine of PMMA@Fe.

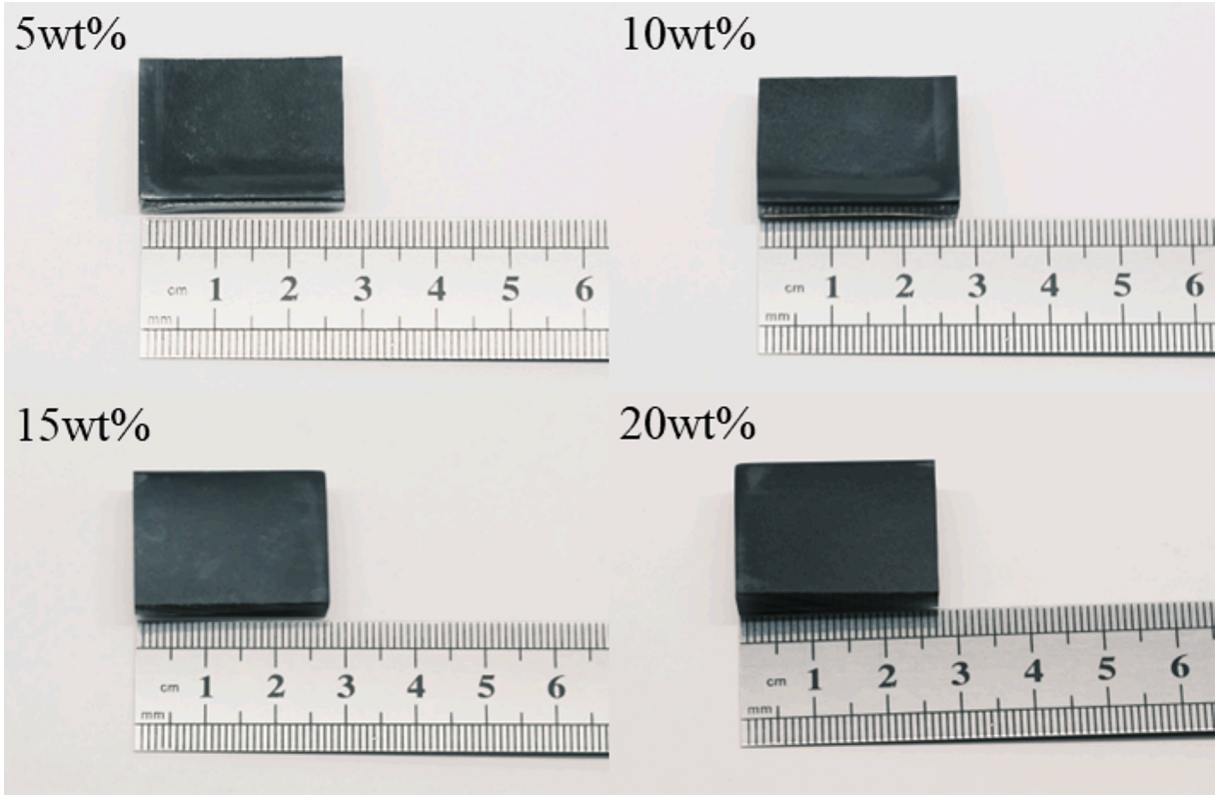

Fig. 5. The different doping ratios (5/10/15/20 wt%) of PMMA@Fe.

Table 2
The density of PMMA@Fe.

Propellant	Weight of iron powder (wt%)	Density (g/cm^3)
PMMA	0	1.20
PMMA@Fe	5	1.23
	10	1.30
	15	1.35
	20	1.43

$$\frac{C_{p,\mathrm{PMMA}} - C_{v,\mathrm{PMMA}}}{C_{p,\mathrm{PMMA}}} = 0.03 \tag{7}$$

According to the experimental results of Lebedev et al. [43], the value of $C_{p,\ \mathrm{PMMA}}$ is determined to be 131.8 (J/mol•K). So the value of $C_{v,\ \mathrm{PMMA}}$, and γ_{PMMA} can be estimated as

$$C_{v,\mathrm{PMMA}} = (1 - 0.03)C_{p,\mathrm{PMMA}} = 92.16(\mathrm{J/mol \bullet K}) \tag{8}$$

Table 3
Experimental conditions of PPT.

Experimental condition	Propellant	Weight of iron powder(wt%)	Energy (J)	Discharge voltage (V)	Operating frequency (Hz)
Case 1	PMMA	0	4.5	2000	1
Case 2	PMMA@Fe	5			
Case 3	PMMA@Fe	10			
Case 4	PMMA@Fe	15			
Case 5	PMMA@Fe	20			

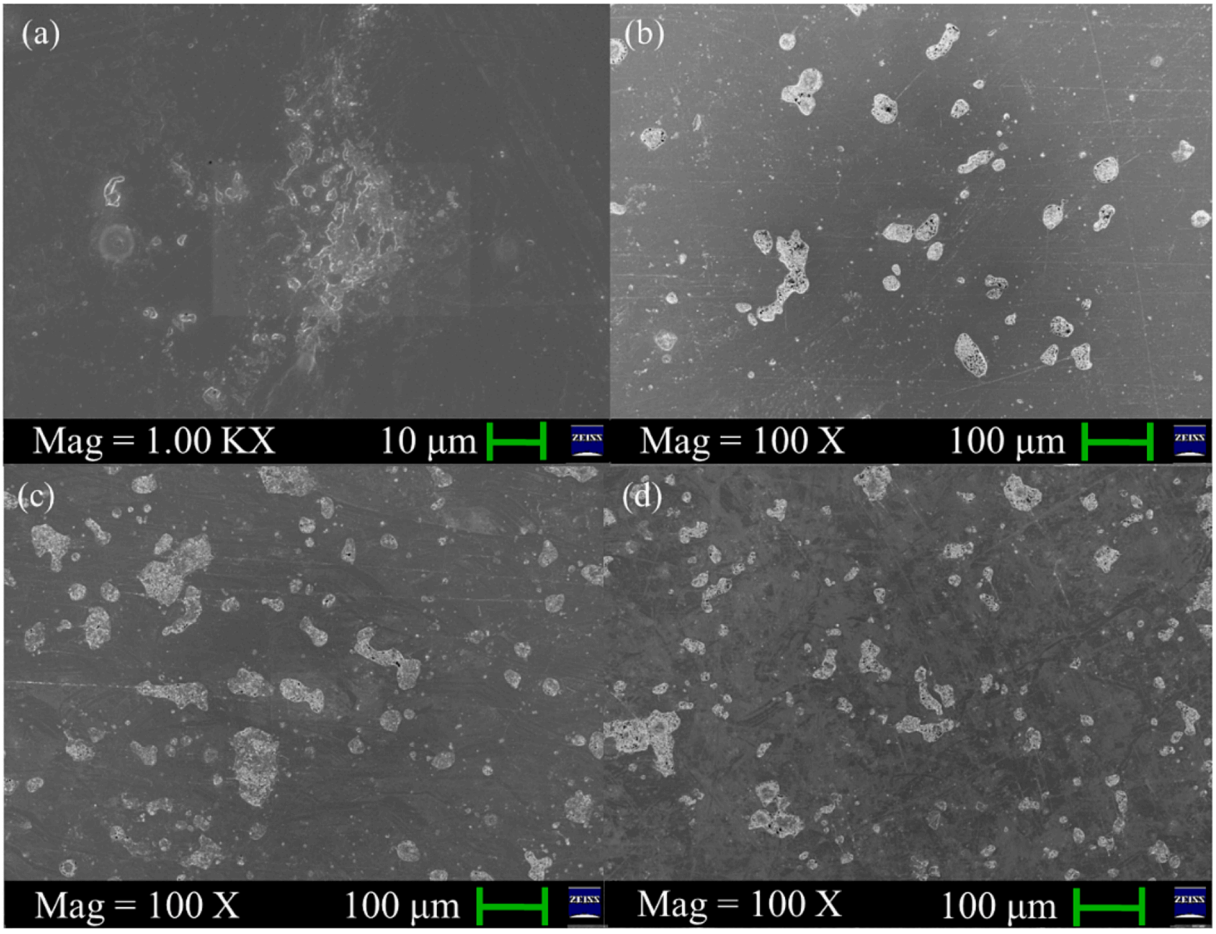

Fig. 6. SEM images of (a) Case 2 (b) Case 3 (c) Case 4 (d) Case 5 before use.

$$\gamma_{PMMA} = \frac{C_{p,\mathrm{PMMA}}}{C_{v,\mathrm{PMMA}}} = 1.43 \tag{9}$$

If we consider the mixture, we need first to determine the original ratio of specific heat (γ) for each component based on their respective proportions. Taking the example of a mixture consisting of 20 g of PMMA mixed with 5 wt% iron, we can use a mass percentage-weighted average to calculate the mixture's γ value.

First, calculate the contribution of each component to γ:

$$Contribution_{PMMA} = M_{PMMA} \times \gamma_{PMMA} \tag{10}$$

$$\mathrm{Contribution}_{Fe} = \mathrm{M}_{Fe} \times \gamma_{Fe} \tag{11}$$

Then, calculate the mixed γ value:

$$\gamma_{Mixed} = \frac{ContributionPMMA + ContributionFe}{Totalmass} \tag{12}$$

In this case, substitute values:

$$\gamma_{Mixed} = \frac{(20g \times 1.43) + (1.053g \times 1.67)}{20g} = 1.51 \tag{13}$$

According to this estimation method, we can effectively define the ratio of specific heats (γ) for mixtures with different weight percentages. This will facilitate subsequent calculations for thrust generated by gas expansion (electrothermal) in the process of PPT.

3.2. Method

To evaluate the propulsion performance of different propellants, we began by characterizing the synthesized materials using SEM-EDS and Micro-CT. Scanning Electron Microscopy with Energy Dispersive Spectroscopy (SEM-EDS) was employed to analyze the surface morphology and elemental composition of the propellant samples. In parallel, Micro-Computed Tomography (Micro-CT) was used to obtain detailed 3D imaging of the propellant's internal structure, enabling the identification of potential voids or inhomogeneities that might affect its performance.

Experimental setups were designed to compare the discharge voltage

Table 4
EDXS analysis of element atom%.

Condition	C(Atom%)	N(Atom%)	O(Atom%)	Fe(Atom%)
Case 1	68.81	2.12	29.07	0.00
Case 2	60.19	2.42	17.47	19.92
Case 3	52.69	2.26	9.2	35.85
Case 4	51.57	0.55	8.45	39.43
Case 5	46.19	0	4.15	49.67

and current of pure PMMA and PMMA@Fe propellants with varying iron powder content. These setups provided insights into the discharge characteristics of the propellants, serving as the basis for calculating the impulse bit using Equation (2). Detailed experimental conditions are listed in Table 2.

Additionally, the plasma plume generated by the PPT was analyzed using a Faraday cup and a spectrometer to understand the effects of iron powder addition on propellant performance. The Faraday cup measured changes in the total charge of the plasma plume, offering insights into plasma quantity. Meanwhile, the optical emission spectrum (OES) was employed to analyze the elemental composition of the plasma plume and assess intensity variations. This approach helped elucidate the contributions of iron powder to the plasma's properties and the overall performance of the propellant.

4. Results and discussion

4.1. Characterization of the PMMA@Fe prepollent

Fig. 6 presents the SEM micrographs of Cases 2 to 5 before use. It can be observed that, as the iron powder doping increases from Case 1 to Case 5, the number of surface pores progressively increases. As inorganic particles are generally more challenging to disperse uniformly within an organic matrix [44], this could lead to localized agglomeration during mixing. These agglomerated regions may subsequently form pores or voids.

EDXS analysis shown in Table 4 confirms the presence of the expected elements (C, O, Fe) in the PMMA@Fe composites. This result aligns with the anticipated elemental composition and proves that the targeted composites were synthesized successfully. Moreover, the analysis reveals a significant increase in the detected Fe content, further confirming the effective incorporation of iron into the PMMA matrix and the successful preparation of the composite material as intended.

4.2. Micro-CT analysis

After confirming the material's elemental composition, further investigation was conducted to examine the internal struct. It was done to verify whether the surface defects observed in the SEM analysis were indeed caused by uneven mixing. Fig. 7 shows the side view of the Micro-CT images for Cases 2 to 5, where the white regions represent iron powder. As the Fe powder mixing ratio increases, the particles settle more significantly at the bottom during the preparation of PMMA@Fe samples due to the higher density of iron powder (7.87 g/cm^3) compared to the PMMA matrix (1.18 g/cm^3), causing rapid downward movement under gravity during the casting process. To avoid experimental interference, no dispersants were added during preparation, which exacerbated particle sedimentation. Dispersants reduce aggregation through electrostatic repulsion or steric hindrance[45], enhancing uniform distribution, but in their absence, Fe particles in PMMA solvent tend to aggregate into larger clusters that settle more

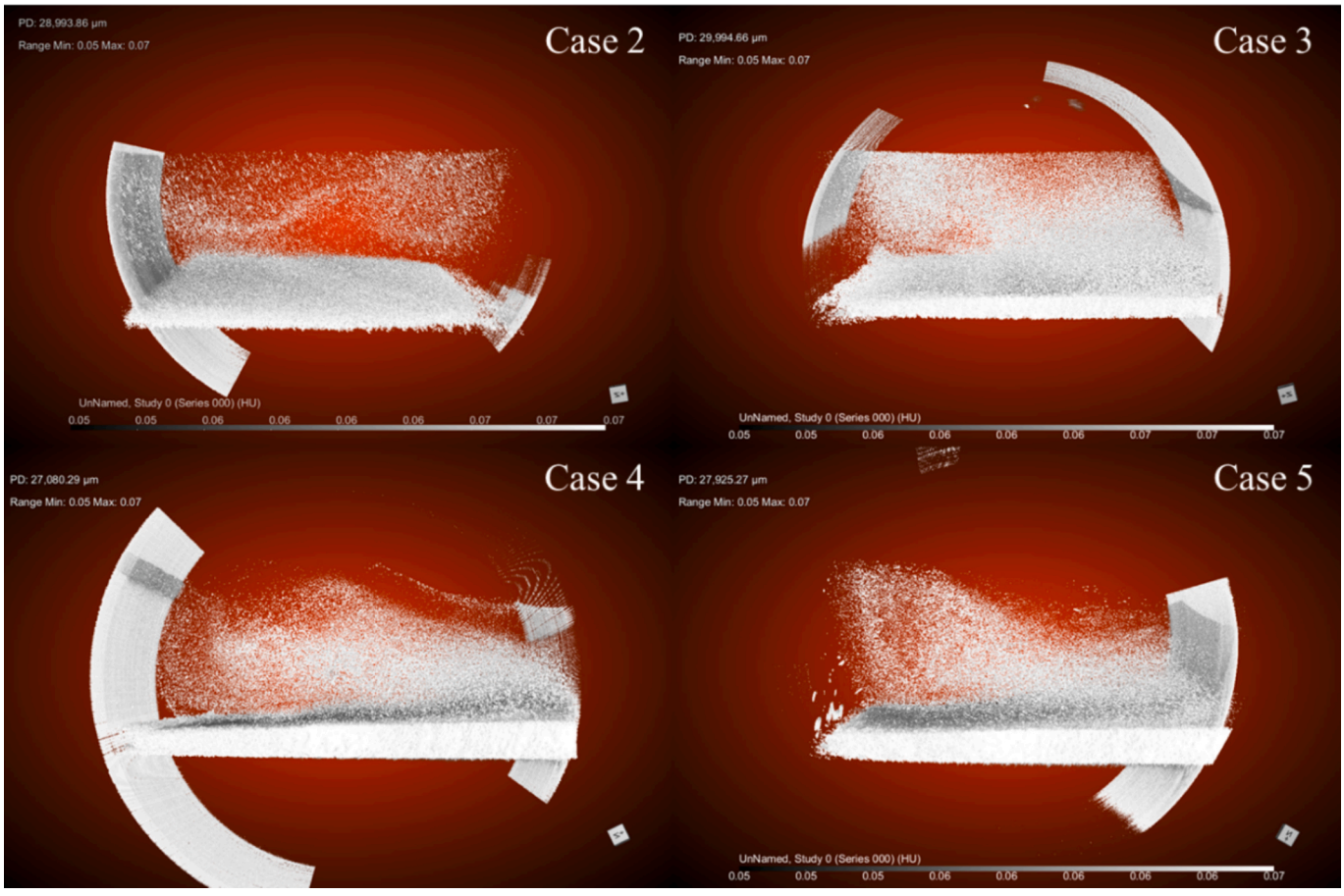

Fig. 7. The side view of the Micro CT image for Case 2 ~ 5.

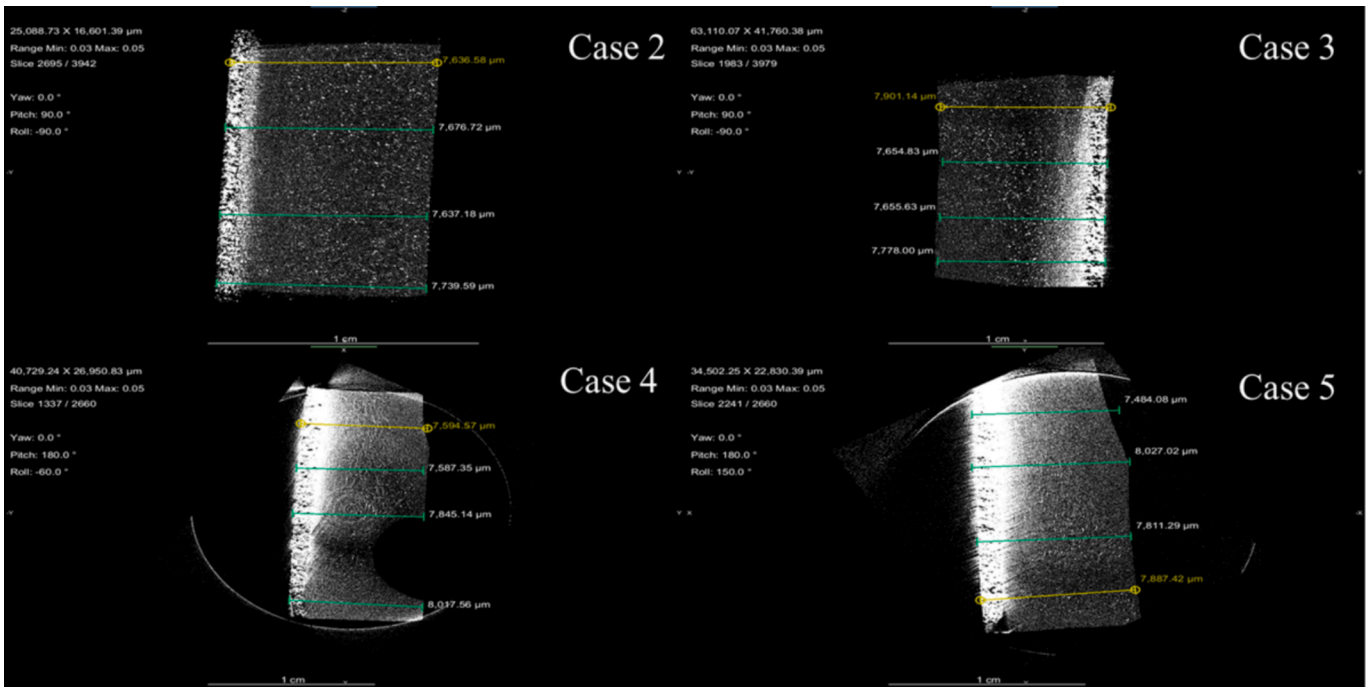

Fig. 8. The sectional view of the Micro CT image for Case 2 ~ 5.

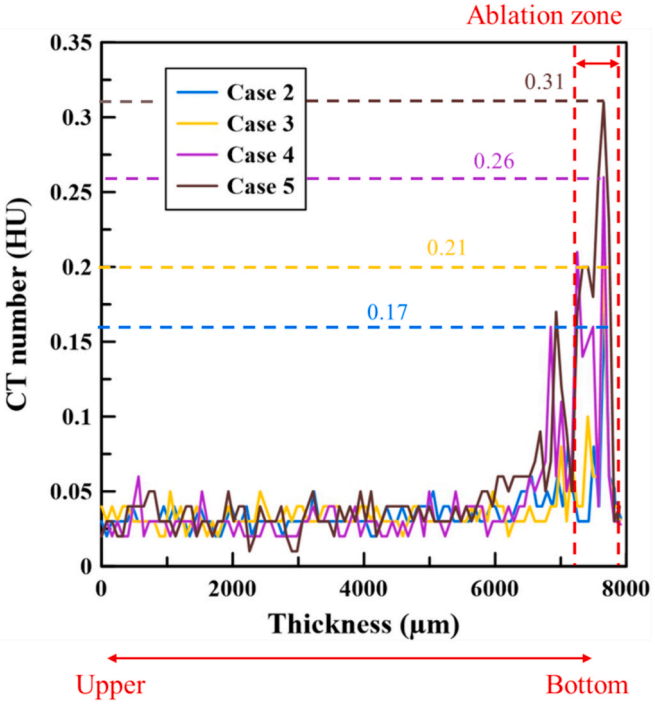

Fig. 9. The CT values of Case 2–5.

rapidly under gravity. The interfacial interactions between inorganic Fe powder and the organic PMMA matrix also influence sedimentation. The high surface energy of Fe powder and its poor chemical compatibility with PMMA hinder uniform dispersion. Higher Fe content increases particle contact, amplifying van der Waals forces and aggregation, which accelerates the sedimentation process.

The sectional view of each case (shown in Fig. 8) was conducted, as the thickness of each sample is approximately 8000 μm. The variation in iron powder content from the top layer to the bottom was determined through the intensity of CT values along the cross-section (shown in Fig. 9). The maximum CT value for each case was consistently observed between 7000 and 8000 μm, with noticeable differences among the cases. By calculating the iron powder mixing ratio from the average CT values and the initial mixing ratio of the raw iron powder, the maximum mixing ratios for Cases 2 to 5 were determined to be 21, 44, 67, and 89 wt%, respectively (listed in Table 5). These results confirm that significant differences and comparability exist between the cases. Based on preliminary estimates, assuming uniform ablation of the propellant and ablation rate is 10 μg/shot, the surface defined as the bottom-most region of the sample could sustain at least 50,000 discharges before reaching the 7000 to 8000 μm range, which we define as the ablation zone.

Table 5
Conversion of CT values to weight percentage for cases 2–5.

	0 wt%	5 wt%	10 wt%	15 wt%	20 % wt
Mean (HU)	–	0.04	0.048	0.058	0.07
Max (HU)	–	0.17	0.21	0.26	0.31
Max wt%	–	**21 %**	**44 %**	**67 %**	**89 %**
Experimentalcondition	Case 1	Case 2	Case 3	Case 4	Case 5

4.3. *Discharge characteristics of PPT with PMMA@Fe*

The discharge voltage and current waveforms for different experimental conditions (Cases 1 to 5) were measured, all obtained under an energy output of 4.5 J. As shown in Fig. 10**(a)**, the discharge voltage waveforms remain largely consistent across all cases. Observing the discharge current in Fig. 10**(b)**, the waveforms display underdamped oscillations, with a significant increase in the peak current observed after adding Fe powder to the PMMA. The peak current reaches its maximum in Case 5, indicating that the addition of Fe powder effectively enhances the plasma characteristics during PPT discharge.

A total of 10,000 discharge experiments were conducted for Cases 1 to 5, during which impulse bit, propellant ablation rate, and various propulsion performance parameters were measured. In the Case 5 experiment, spontaneous breakdown was observed at 2,000 V without

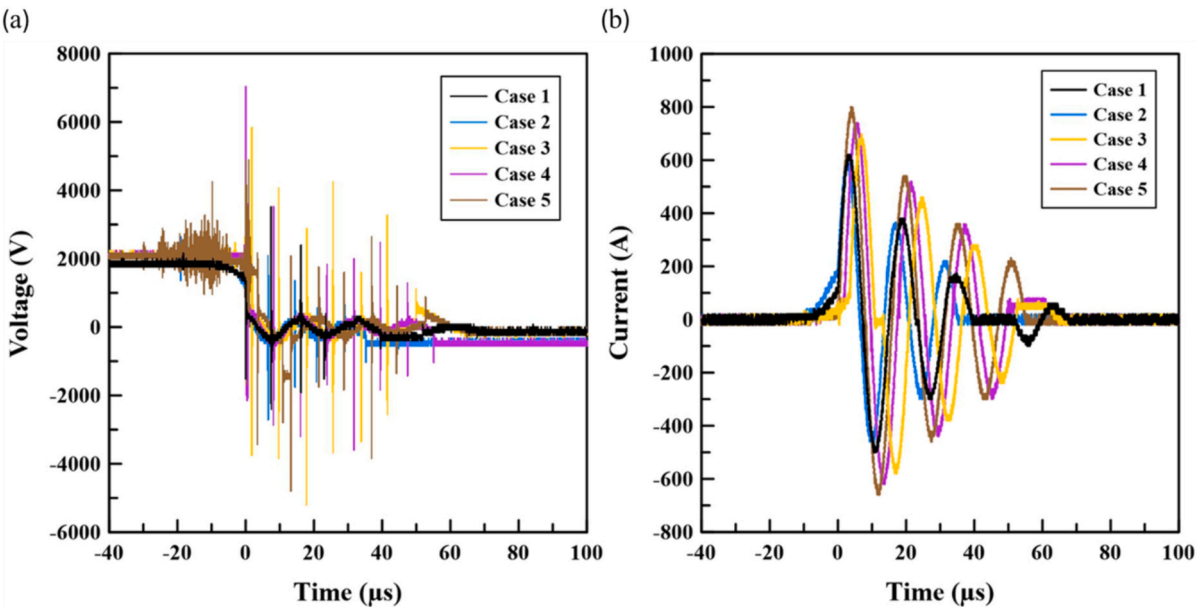

Fig. 10. (a) The discharge voltage waveform with different conditions. (b) The discharge current waveform with different experimental conditions.

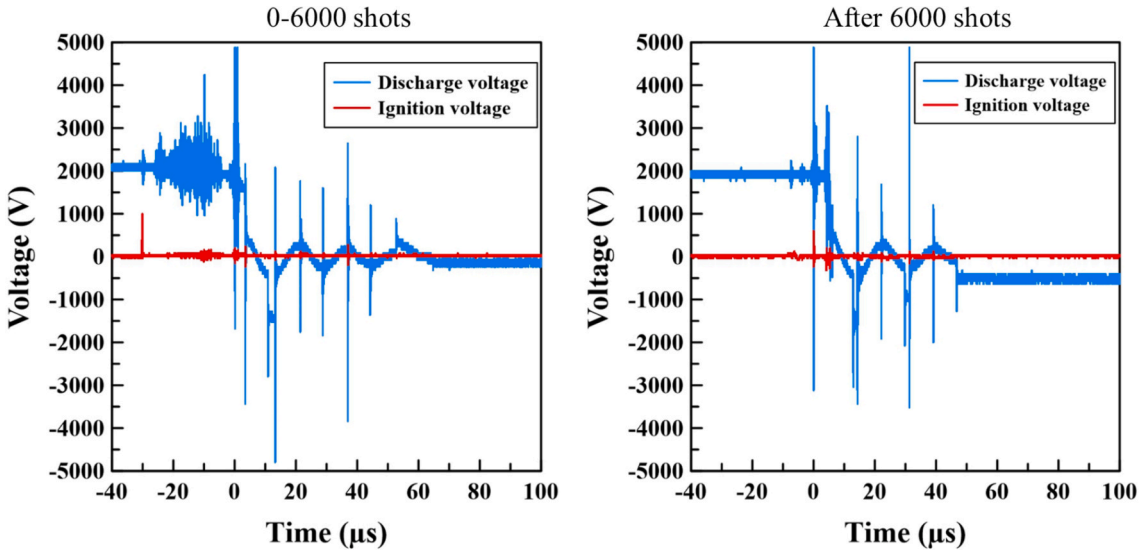

Fig. 11. Discharge and ignition voltage comparison before and after 6000 shots in case 5.

the igniter providing initial plasma after 6,000 discharges, as shown in Fig. 11. This phenomenon aligns with findings by EUN-SUB LIM et al. (2006), who reported that adding 4.5 % Ni to a 2 mm PMMA-Ni film drastically increased its conductivity and dielectric constant due to the formation of conductive clusters merging into infinite clusters, transforming the system from non-conductive to conductive [46].

Dielectric constants for Cases 1 to 5 were subsequently measured and compared. As illustrated in Fig. 12, the dielectric constant increased with iron powder content, indicating a decline in insulation properties. While the increase in the dielectric constant for PMMA@Fe was not drastic, this may be attributed to differences in sample thickness across the cases.

After 6,000 discharges in Case 5, substantial deposits were identified within the internal structure of the PPT, as shown in Fig. 13. These deposits are conjectured to consist of carbon and metals, based on the known ablation processes during PPT discharge. Non-accelerated plasma undergoes electron recombination, converting into atoms that deposit onto the propellant walls. Since the PMMA@Fe propellant contains carbon (C) and iron (Fe), and the electrodes are made of copper (Cu), the deposits are likely composed of these elements.

This accumulation of deposits explains the irregular discharges observed in Case 5. After 6,000 discharges, the breakdown voltage between electrodes dropped below 2,000 V, resulting in uncontrolled discharge frequencies. This irregular behavior poses significant risks to the power supply, as excessive current and voltage fluctuations may exceed the system's rated capacity, potentially triggering overload protection mechanisms or causing permanent damage to internal components.

Consequently, the operational lifespan of the PPT system using Case 5 conditions is limited to 6,000 discharges. All subsequent experimental data for Case 5 are therefore based on this reduced discharge count.

4.4. Effect of iron powder content on the ablation rate of PMMA-base propellants

In this experiment, a precision electronic balance (AP324X,

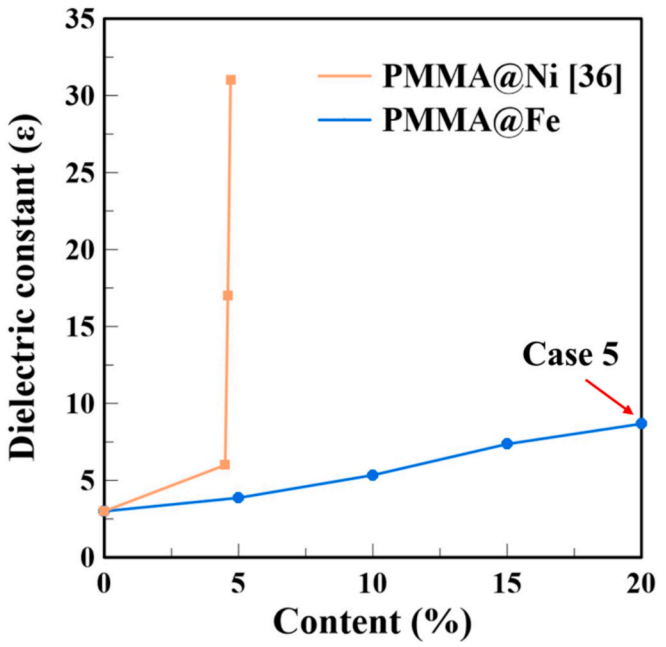

Fig. 12. Relationship between dielectric constant and metal doping content in PMMA.

Shimadzu, Japan) is used. The electronic balance has a maximum precision of 0.0001 g, allowing for accurate measurement of the mass change of the propellant before and after the experiment. Additionally, the Arduino's counting function records the number of thruster firings and performs calculations to obtain the average mass change of the propellant consumed during each discharge.

Fig. 14 illustrates the average ablation rate for each experimental condition, demonstrating a clear correlation between the iron powder weight ratio in PMMA@Fe propellants and the ablation rate. Comparing Case 1 (pure PMMA) and Case 2 (5 wt% Fe), the average ablation rate increased from 4.6 μg/shot to 8.2 μg/shot, reflecting an approximately 80 % enhancement. For Cases 2 through 5, the increase was more gradual, with each additional increment in iron powder content resulting in an approximate 10 % rise.

This data indicates that the inclusion of Fe powder significantly enhances the ablation rate of the propellant. Based on current waveform measurements, the observed increase in maximum current values is a key contributor to this effect. The Joule heating effect, driven by higher current, leads to greater heat accumulation on the propellant surface, accelerating the ablation process.

Moreover, the lower first ionization energy of iron (7.87 eV) compared to carbon (11.26 eV) and oxygen (13.62 eV) in PMMA facilitates the generation of more plasma during PPT discharges. This enhancement in plasma production increases the frequency of particle collisions, further boosting the propellant's ablation rate.

4.5. *Impact of iron doping on impulse bit in PMMA-based PPT propellants*

With the current waveforms and propellant ablation rate data, the electromagnetic (EM) impulse bit and electrothermal (ET) impulse bit were calculated using Equations (2) and (3), respectively. Fig. 15 compares the electromagnetic and electrothermal impulse bits. In this study, more than 90 % of the PPT thrust is attributed to electrothermal forces. Both electromagnetic and electrothermal forces increase with higher iron powder content. The total impulse bit of Case 2 is approximately 37.5 % higher than that of Case 1, while Case 5 shows a 62.5 % increase compared to Case 1, reaching approximately 130 μN•s. These results demonstrate that the addition of Fe powder significantly enhances the impulse bit of the thruster.

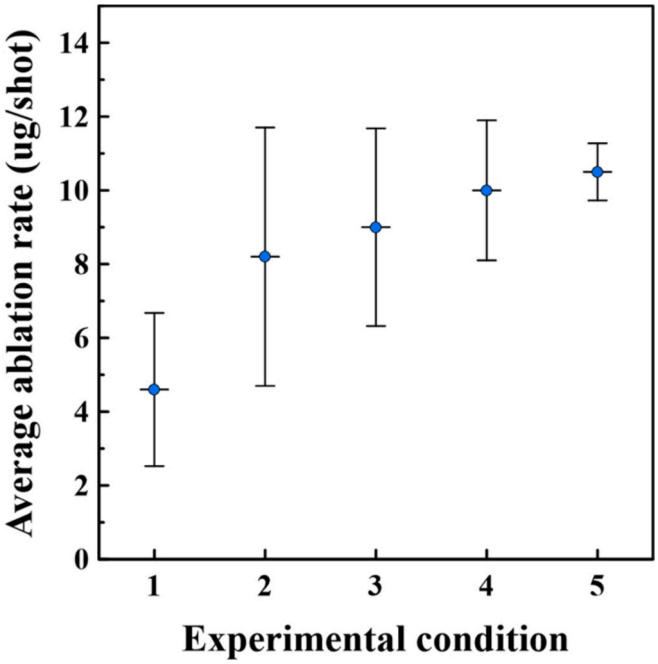

Fig. 14. The average ablation rate for each condition.

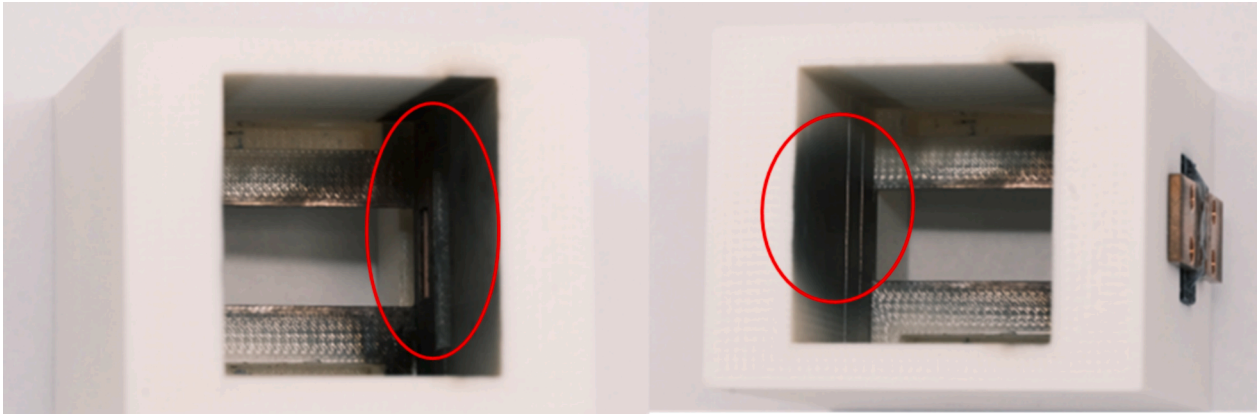

Fig. 13. Carbon and metal deposition on both sides of the thruster interior after 6000 shots in case 5.

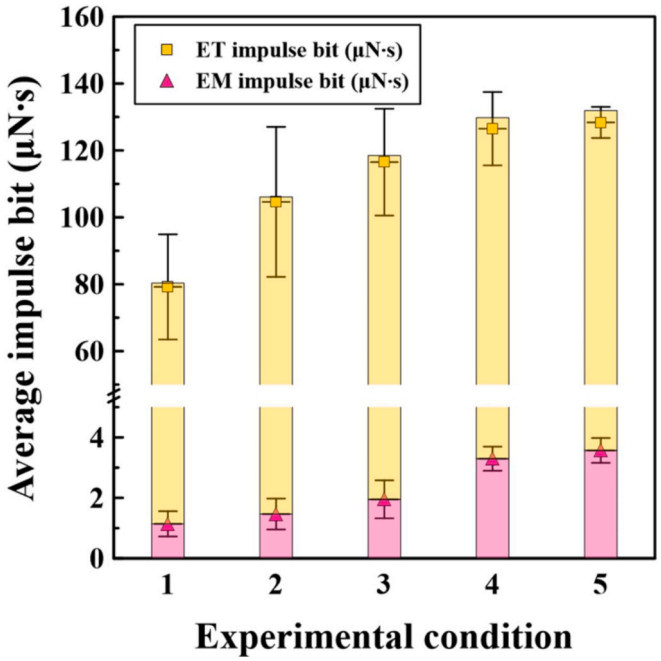

Fig. 15. Comparison of the relationship between electromagnetic impulse bit and electrothermal impulse bit with different experimental conditions.

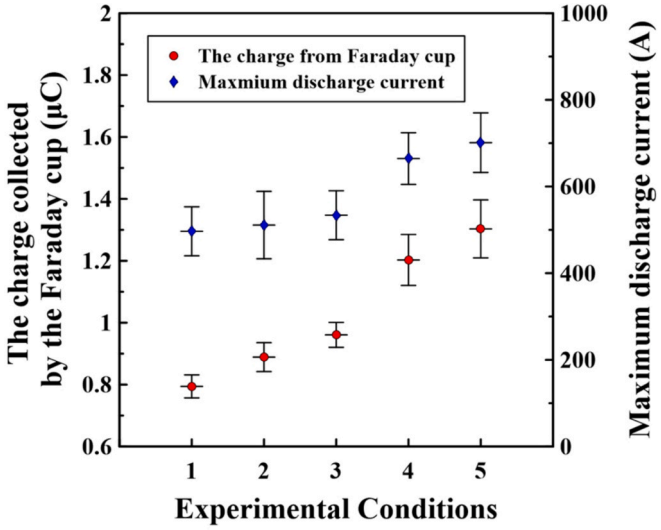

Fig. 16. Comparison between the charge collected by the Faraday cup and the maximum discharge current with different experimental conditions.

4.6. Faraday cup measurements under varying experimental conditions (Case 1 ~ 5)

Based on the previous results, to further understand the effect of iron powder in PMMA@Fe propellants, a Faraday cup was placed 10 cm from the PPT outlet to collect and analyze the plasma plumes generated under different experimental conditions. Due to the complexity of the plasma composition produced by PMMA@Fe propellants, estimating the plasma density directly is challenging. Instead, the total charge (Q) collected is used as an indicator of the plasma generated during PPT discharges. Although Q is primarily derived from the ions involved in the discharge process, it is indirectly related to plasma density. By measuring the current and integrating it over time, the total charge can indirectly reflect the scale magnitude and intensity of plasma generation during discharges. Therefore, total charge serves as a reliable indicator of plasma production. The total charge is calculated by measuring the voltage drop across a resistor, converting it to ion current, and integrating the time-dependent ion current I(t).

$$Q = \int I(t)dt \tag{14}$$

According to Ohm's law, the relationship between current (I), voltage (V), and impedance (Z) can be expressed as:

$$I = V/Z \tag{15}$$

Fig. 16 compares the charge measured by a Faraday cup and the maximum discharge current under different conditions. Experimental data reveal that as the iron powder content increases, the amount of charge collected from the plasma plume also rises. This indicates that the addition of iron powder enhances the overall plasma generation, thereby reducing impedance and leading to higher discharge currents. At the same energy input with a fixed voltage of 2000 V, PMMA propellants with higher iron powder concentrations exhibit increased discharge currents, consistent with the previously observed trend of rising current values.

Additionally, Time of Flight (TOF) was utilized to measure the velocity of the plasma plume. An oscilloscope was used to simultaneously record the discharge current and the ion current collected by the Faraday cup. By comparing the peak values of the two signals, the time difference (Δt) was determined. Using the known distance (D) between the Faraday cup and the thruster along with the measured time difference, the plasma plume velocity was calculated as shown in Fig. 17.

According to the Lorentz force:

$$\vec{F} = q\left(\vec{E} + \vec{v} \times \vec{B}\right) \tag{16}$$

When the electric field $\vec{E}$ has minimal influence, the magnetic field $\vec{B}$ primarily drives the force:

$$\vec{F} \approx q\left(\vec{v} \times \vec{B}\right) \tag{17}$$

According to Newton's second law, the acceleration of a particle is related to the magnitude of the Lorentz force:

$$m\vec{a} = q\left(\vec{v} \times \vec{B}\right) \Rightarrow a = \frac{qvB}{m} \tag{18}$$

The relationship between acceleration and velocity shows that under the influence of the Lorentz force, the change in particle velocity can be expressed as:

$$v(t) = v_0 + \int a(t)dt \tag{19}$$

With acceleration given by $= \frac{qvB}{m}$, the velocity can be derived as:

$$v(t) = v_0 \exp\left(\frac{qB}{m}t\right) \tag{20}$$

$$v(t) \propto qB \tag{21}$$

This indicates that the particle velocity increases exponentially over time due to the Lorentz force, which is positively correlated with the magnetic field (B) and charge (q). Fig. 18 compares plasma velocity and electromagnetic impulse bit under different experimental conditions. The plasma velocity with each case was measured 10 times. The induced magnetic field generated by higher discharge currents further enhances the Lorentz force, as previously confirmed in earlier experiments. The strengthening of the Lorentz force accelerates the charged particles within the thruster more effectively, explaining why both the EM impulse bit and plasma velocity exhibit a positive correlation with increasing iron powder doping.

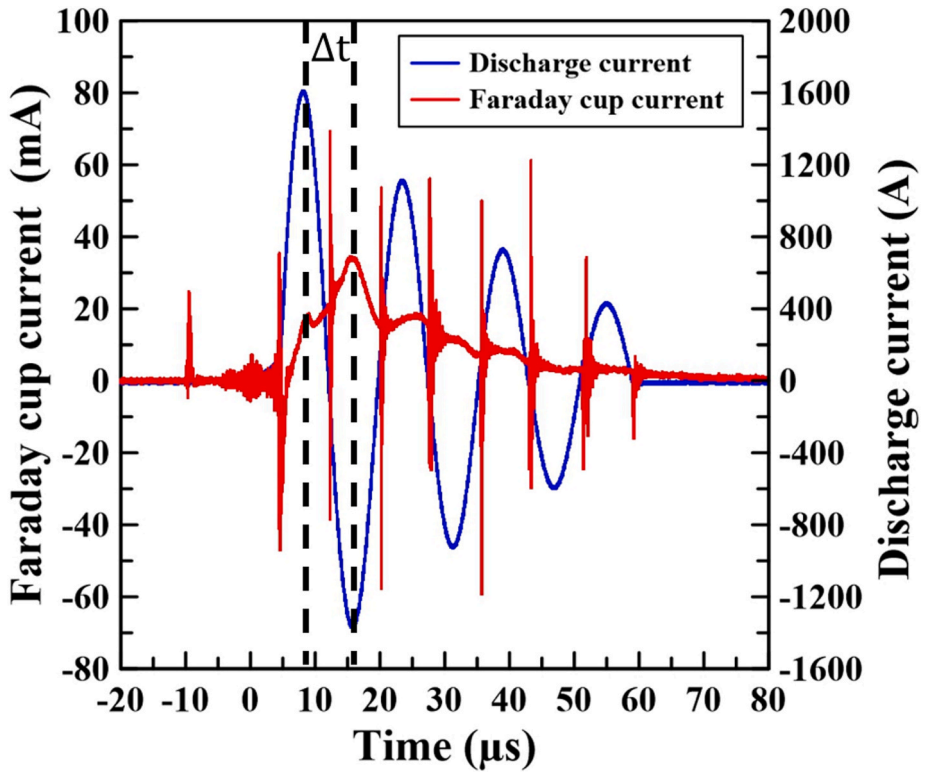

Fig. 17. Comparing the time difference between the maximum discharge current and the Faraday cup signal.

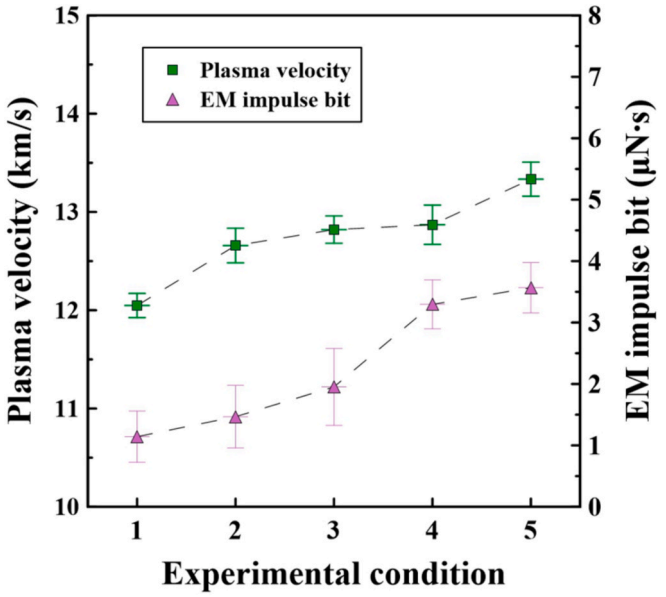

Fig. 18. Comparing the plasma velocity and electromagnetic impulse bit with different experimental condition cases.

4.7. Optical emission spectrum under varying experimental conditions (Case 1 ~ 5)

The previous experimental results demonstrated that adding iron powder to PMMA as a propellant effectively increases the ablation rate and enhances overall plasma generation. To further confirm whether this effect is due to the addition of iron powder itself or simply the increase in material quantity, a spectrometer was used to analyze the plasma plume produced by the PPT. As shown in Fig. 19, the optical emission spectra under different experimental conditions reveal that most of the emission peaks originate from C, H, O, and Fe elements, and their molecular species, which are generated by the ablation and decomposition of PMMA containing iron powder $(C_5O_2H_8)_n$. Additionally, Cu emission peaks from electrode material evaporation were observed, indicating that the electrodes significantly influence plasma composition during the discharge process.

To compare the intensities of various elements and molecules across Cases 1–5, Fig. 20 presents the emission intensities as percentages, with the x-axis listing key molecules such as CH, CO, and C_2, all of which are products of PMMA decomposition. The increased intensity of these molecules indirectly reflects the rise in plasma generation from PMMA decomposition. The results show a progressive increase in the percentage intensity of these molecules as the iron powder content increases from Case 1 to Case 5. In Case 1, the molecular intensities account for less than 10 %. In Case 2, they rise to 10–15 %; in Case 3, further to 15–20 %; in Case 4, approximately 20 % or higher; and in Case 5, the molecular intensity reaches its peak at around 40 %. These findings confirm that the addition of iron powder promotes PMMA ablation and decomposition, resulting in enhanced plasma production. Furthermore, the results indicate that the increase in plasma generation is not solely due to the presence of iron powder but also because the iron powder effectively accelerates PMMA decomposition. This aligns with the observations of increased plasma plume charge measured by the Faraday cup.

4.8. Thruster performance

Fig. 21 presents the specific impulse and thrust efficiency of the PPT under conditions from Case 1 to Case 5. In PMMA@Fe propellants, the specific impulse increases as the iron powder content decreases. Case 1 (pure PMMA) achieves the highest specific impulse, approximately 1781 s, while Case 5 shows the lowest, about 1282 s. This is due to the addition of iron powder, which increases the ablation rate of the propellant. However, the improvement in impulse bit is not as significant,

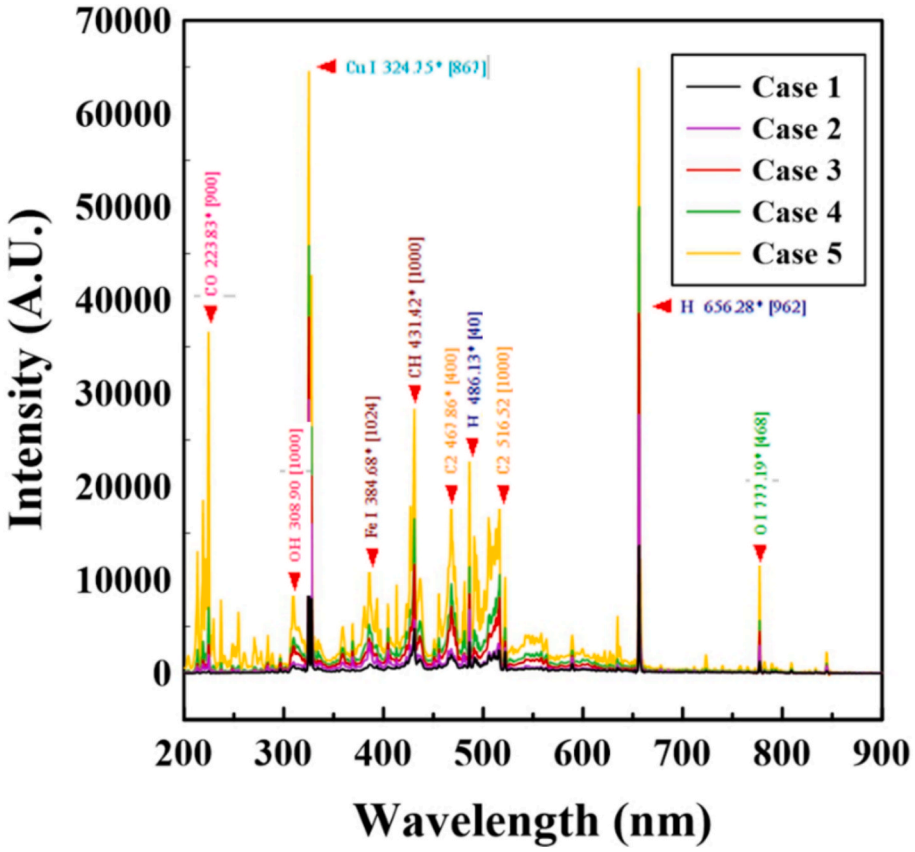

Fig. 19. The optical emission spectrum of PPT in Case 1 ~ 5.

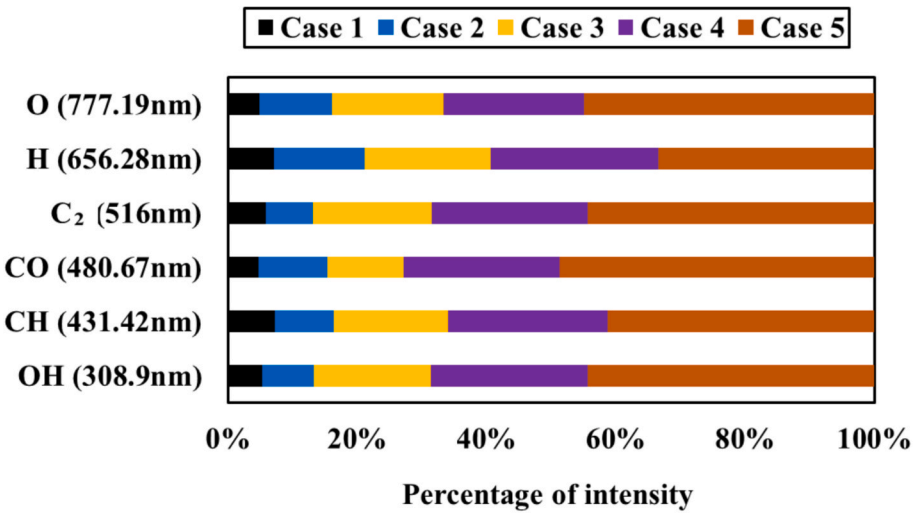

Fig. 20. Percentage of emission intensities for elements and molecules in Case 1 ~ 5.

resulting in a decrease in specific impulse as the iron powder content increases. Regarding thrust efficiency, Case 1 exhibits the lowest efficiency at 15.6 %, but with the addition of iron powder, the efficiency reaches its peak in Case 4 at approximately 18.7 %. However, when the iron powder content increases further in Case 5, the efficiency does not continue to improve as expected; instead, it drops to 18.4 %. This is primarily due to the increased carbon–metal deposition during the discharge process, particularly on the electrode surfaces, which reduces insulation performance and disrupts the electric field distribution, leading to unstable discharges. Additionally, the increased current associated with higher iron content generates excessive heat, resulting in inefficient thermal dissipation and further reducing the system's energy utilization. These combined factors contribute to the decline in thrust efficiency at higher iron powder concentrations. For the thrust-to-power ratio, this parameter gradually increases with iron powder content, reaching its maximum value of 29.3 μN/J in Case 5. Detailed performance data for the PPT are listed in Table 6.

Considering the limited lifespan of 6000 shots when using Case 5, despite its superior performance in I_{bit} and thrust-to-power ratio, Case 4 is recommended as the optimal configuration. This is due to its highest

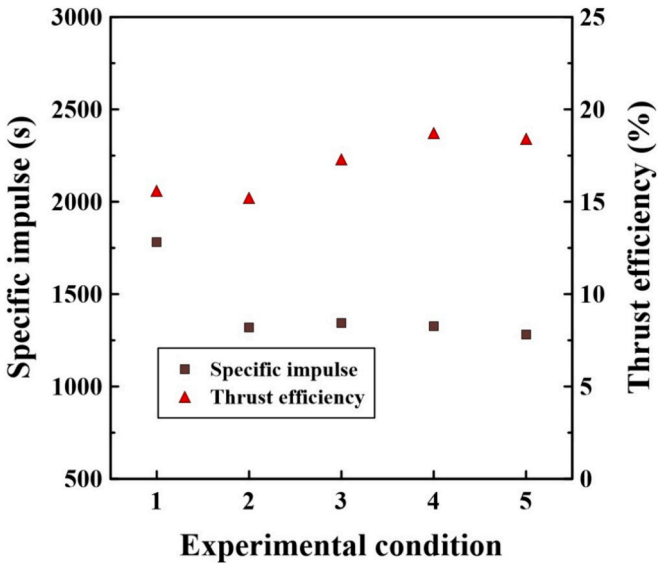

Fig. 21. The specific impulse and thrust efficiency of PPT in case 1 ~ 5.

Table 6
PPT performance parameter in case 1 ~ 5.

Condition	I_{sp} (s)	I_{bit} (μNs)	η_t (%)	Thrust-to-power ratio (μN/J)
Case 1	1781	80.3	15.6	17.8
Case 2	1319	106	15.2	23.6
Case 3	1342	118.4	17.3	26.3
Case 4	1324	129.8	18.7	28.8
Case 5	1282	131.9	18.4	29.3

thrust efficiency, similar impulse performance to Case 5, and a specific impulse approximately 3 % higher than Case 5.

In summary, the results indicate that when the iron powder content increases from Case 4 to Case 5, the improvements in propulsion parameters become negligible or even regress in some metrics. Therefore, considering both the propulsion performance and the operational lifespan, Case 4 offers a more favorable balance and is identified as the preferred option.

5. Conclusion

In this study, we investigated the effects of iron powder (Fe) content in PMMA-based propellants (PMMA@Fe) on propulsion performance, plasma generation, and material ablation. The results showed that the addition of iron powder significantly enhances the ablation rate, with the highest increase observed in Case 5. Faraday cup measurements revealed a direct correlation between the iron powder content and the total charge collected, indicating that higher Fe concentrations lead to increased plasma generation, which in turn reduces impedance and enhances discharge currents. The spectrum analysis confirmed that the increase in plasma intensity is primarily due to the enhanced ablation of PMMA facilitated by iron powder, with a noticeable increase in the emission intensity of PMMA-derived molecules.

Furthermore, impulse bit measurements (I_{bit}) and thrust efficiency were found to be positively influenced by the presence of iron powder. While specific impulse was highest in Case 1 (pure PMMA), Case 4 demonstrated the best balance between thrust efficiency and performance, surpassing Case 5 in terms of efficiency and specific impulse despite its lower overall specific impulse. The findings suggest that adding iron powder to PMMA propellants improves plasma generation and propulsion performance, with Case 4 offering the most optimal balance between thrust and efficiency.

CRediT authorship contribution statement

Chao-Wei Huang: Conceptualization, Data curation, Funding acquisition, Project administration, Supervision. **Ping-Han Huang:** Writing – original draft, Validation, Software, Investigation, Data curation. **Zong-Ying Yang:** Writing – original draft, Software, Investigation, Formal analysis, Data curation. **Yueh-Heng Li:** Supervision, Resources, Project administration, Funding acquisition, Conceptualization.

Declaration of competing interest

The authors declare that they have no known competing financial interests or personal relationships that could have appeared to influence the work reported in this paper.

Acknowledgments

This study was financially supported by the National Science and Technology Council (Taiwan) under Grant Nos. NSTC 112-2628-E-006-005-MY3, NSTC 113-2223-E-006-010, and NSTC 113-2218-E-006-020.

Data availability

Data will be made available on request.

References

[1] F.-T. Hwang, Mission Design and Analysis for FORMOSAT-7 Program, in: 14th International Conference on Space Operations, 2016, pp. 2441.
[2] E. Adams, D. O'Shaughnessy, M. Reinhart, J. John, E. Congdon, D. Gallagher, E. Abel, J. Atchison, Z. Fletcher, M. Chen, Double asteroid redirection test: The earth strikes back, in: 2019 IEEE Aerospace Conference, IEEE, 2019, pp. 1-11.
[3] R.H. Frisbee, Advanced space propulsion for the 21st century, J. Propul. Power 19 (2003) 1129–1154.
[4] S. Mazouffre, Electric propulsion for satellites and spacecraft: established technologies and novel approaches, Plasma Sources Sci. Technol. 25 (2016) 033002.
[5] D. Krejci, P. Lozano, Space propulsion technology for small spacecraft, Proc. IEEE 106 (2018) 362–378.
[6] D. Lev, R.M. Myers, K.M. Lemmer, J. Kolbeck, H. Koizumi, K. Polzin, The technological and commercial expansion of electric propulsion, Acta Astronaut. 159 (2019) 213–227.
[7] Y.-H. Li, T.-Y. Huang, M.M. Shen, Y.-C. Chen, Development of Miniature Radio Frequency Ion Thruster with Inductively Coupled Plasma Source, Journal of Aeronautics, Astronautics and Aviation 55 (2023) 13–28.
[8] Y.-H. Li, Y.-C. Chen, S.-W. Liu, A.R. Aslan, Prediction and optimization of thrust performance from plasma diagnostics in the inductively coupled plasma of an RF ion thruster, Acta Astronaut. 208 (2023) 130–141.
[9] J.-P. Boeuf, Tutorial: Physics and modeling of Hall thrusters, J. Appl. Phys. 121 (2017).
[10] J.H. Hsieh, Y.-H. Li, Review of Hollow Cathode Discharge: Exploring Advanced Design and Optimization, Journal of Aeronautics, Astronautics and Aviation 55 (2023) 385–413.
[11] J.H. Hsieh, Y.-L. Huang, P.-H. Huang, Y.-H. Li, Investigation of anode diameter and keeper geometry influence on open-end emitter heaterless hollow cathode discharge, Vacuum 229 (2024) 113504.
[12] J.H. Hsieh, P.-H. Huang, Y.-L. Huang, H. Juwantono, Y.-H. Li, Analysis of anode surface roughness influence on heaterless hollow cathode discharge, Phys. Scr. 99 (2024) 035607.
[13] J.H. Hsieh, M.M. Shen, Y.-H. Li, P.-H. Huang, Development of a lanthanum hexaboride hollow cathode for a magnetic octupole thruster, Vacuum 214 (2023) 112146.
[14] G. Krulle, M. Auweter-Kurtz, A. Sasoh, Technology and application aspects of applied field magnetoplasmadynamic propulsion, J. Propul. Power 14 (1998) 754–763.
[15] I. Nason, J. Puig-Suari, R. Twiggs, Development of a family of picosatellite deployers based on the CubeSat standard, in: Proceedings, IEEE Aerospace Conference, IEEE, 2002, pp. 1-1.
[16] Y.-H. Li, S. Palagiri, P.-Y. Chang, C. Montag, G. Herdrich, Plasma behavior in a solid-fed pulsed plasma thruster, J. Aeronaut. Astronaut. Aviat 51 (2019) 31–42.
[17] E. Kulu, What Is a CubeSat & Other Picosatellites? , in, Nanosats Database., 2022.
[18] A.M. Pérez, M. Coletti, S. Gabriel, Development of a microthruster module for nanosatellite applications, in: Proceedings of the 32nd International Electric Propulsion Conference, Wiesbaden, Germany, 2011, pp. 11-15.
[19] K. Lemmer, Propulsion for cubesats, Acta Astronaut. 134 (2017) 231–243.

[20] M. Coletti, S. Ciaralli, S.B. Gabriel, PPT development for nanosatellite applications: experimental results, IEEE Trans. Plasma Sci. 43 (2014) 218–225.
[21] A. Nawaz, R. Albertoni, M. Auweter-Kurtz, Thrust efficiency optimization of the pulsed plasma thruster SIMP-LEX, Acta Astronaut. 67 (2010) 440–448.
[22] S. Ciaralli, M. Coletti, S. Gabriel, Results of the qualification test campaign of a Pulsed Plasma Thruster for Cubesat Propulsion (PPTCUP), Acta Astronaut. 121 (2016) 314–322.
[23] B.C. Inc., Bmp-200 Micro-Pulsed Plasma Thruster, in, Busek Co. Inc., 2019.
[24] J. Aoyagi, M. Mukai, Y. Kamishima, T. Sasaki, K. Shintani, H. Takegahara, T. Wakizono, M. Sugiki, Total impulse improvement of coaxial pulsed plasma thruster for small satellite, Vacuum 83 (2008) 72–76.
[25] T. Edamitsu, H. Tahara, Performance measurement and flowfield calculation of an electrothermal pulsed plasma thruster with a propellant feeding mechanism. In: Proceedings of the 29th International Electric Propulsion Conference, 2005.
[26] F. Rysanek, R. Burton, Effects of geometry and energy on a coaxial Teflon pulsed plasma thruster, in, 36th AIAA/ASME/SAE/ASEE Joint Propulsion Conference and Exhibit (2000) 3429.
[27] T.E. Markusic, K.A. Polzin, E.Y. Choueiri, M. Keidar, I.D. Boyd, N. Lepsetz, Ablative Z-pinch pulsed plasma thruster, J. Propul. Power 21 (2005) 392–400.
[28] W. Guman, Pulsed plasma technology in microthrusters, Fairchild Hiller Corp., Farmingdale, NY, AFAPL-TR-68-132, (1968).
[29] Y.-H. Li, K. Dorn, H.-C. Hsieh, T.-C. Kuo, Y.-C. Hsu, Effect of electrode angle on pulsed plasma thruster performance, Journal of Aeronautics, Astronautics and Aviation 53 (2021) 353–367.
[30] D.J. Palumbo, W.J. Guman, Effects of propellant and electrode geometry on pulsed ablative plasma thruster performance, J. Spacecr. Rocket. 13 (1976) 163–167.
[31] S.J. Pottinger, D. Krejci, C.A. Scharlemann, Pulsed plasma thruster performance for miniaturised electrode configurations and low energy operation, Acta Astronaut. 68 (2011) 1996–2004.
[32] K. Hisatsune, Y. Matsumoto, H. Ohisa, T. Tachibana, Use of composite propellants as for electric thrusters, in, International Electric Propulsion Conference, IEPC Paper (1999).
[33] Y.-H. Li, C. Royer, Effect of voltage on second-stage electrodes of dual-stage solid propellant pulsed plasma thruster, Vacuum 167 (2019) 103–112.
[34] H. Tahara, T. Edamitsu, H. Sugihara, Performance Characteristics of Electrothermal Pulsed Plasma Thrusters with Insulator-Rod-Arranged Cavities and Teflon-Alternative Propellants, in: Proceedings of the 30th International Electric Propulsion Conference (IEPC-2007-337), Florence, Italy, 2007, pp. 17-20.
[35] M.S. Glascock, J.L. Rovey, K.A. Polzin, Impulse and performance measurements of electric solid propellant in a laboratory electrothermal ablation-fed pulsed plasma thruster, Aerospace 7 (2020) 70.
[36] H. Mashidori, A. Kakami, T. Muranaka, T. Tachibana, A coaxial pulsed plasma thruster using chemical propellants, Vacuum 80 (2006) 1229–1233.
[37] D. Hou, W. Zhao, X. Kang, P. Wang, Effect of ceramic nozzle on performance of pulsed plasma thruster, Aerosp. Sci. Technol. 12 (2008) 573–578.
[38] M.Y. Junichiro Aoyagi, Taiyo Tezuka, Rin Watanabe, Takayoshi Otsuki, and Shinji Takeya, Series Development of Coaxial Pulsed Plasma Thruster from 1 J to 8 J, in: The 38th International Electric Propulsion Conference, Pierre Baudis Convention Center • Toulouse, France, 2024.
[39] P.H. Huang, S.X. Chang, B.Y. Lai, J.H. Hsieh, Y.-H. Li, Characterization of Vacuum Arc Thruster with Multi-layer Insulator at Different Delay Times of Double Pulses, (2024).
[40] Y.-H. Li, J.-Y. Pan, G. Herdrich, Design and demonstration of micro-scale vacuum cathode arc thruster with inductive energy storage circuit, Acta Astronaut. 172 (2020) 33–46.
[41] P.-H. Huang, Y.-H. Li, T.-Y. Yang, T.-Y. Huang, J.H. Hsieh, J. Heri, Design of the Faraday cup for a Multi-Layer Insulator Vacuum Arc Thruster Characterization, in: In: 2023 IEEE International Conference on Aerospace Electronics and Remote Sensing Technology (ICARES), 2023, pp. 1–6.
[42] C.L. Choy, The heat capacity difference C − C for polymers, J. Polym. Sci. Polym. Phys. Ed. 13 (1975) 1263–1267.
[43] B. Lebedev, I. Rabinovich, Heat capacities and thermodynamic functions of methyl methacrylate and poly (methyl methacrylate), Tr Khim Khim Tekhnol 1 (1971) 8–11.
[44] H. Yaoxing, M. Xinsheng, C. Hongming, Z. Haiying, W. Qiufang, Morphological study and thermal analysis of surface modified α-FeOOH via in situ polymerization of methyl methacrylate, Mater. Res. Bull. 39 (2004) 1159–1166.
[45] G.-H. Zhang, N. Zhu, Y.-B. Li, J.-F. Zhu, Y.-R. Jia, L. Ge, Influence of side-chain structure of polycarboxylate dispersant on the performance of coal water slurry, Fuel Process. Technol. 161 (2017) 1–7.
[46] E.-S. Lim, J.-C. Lee, J.-J. Kim, E.-T. Park, Y.-K. Chung, H.-Y. Lee, Dielectric characteristics of polymer-ceramic-metal composites for the application of embedded passive devices, Integr. Ferroelectr. 74 (2005) 53–60.
[47] Y.-L. Huang, J.H. Hsieh, W.-C. Wang, Y.-H. Li, Investigation of discharge voltage characteristics of a lanthanum hexaboride heaterless hollow cathode, Acta Astronaut. 226 (2025) 760–771.